I

METHODOLOGY BASED ON FBG SENSORS FOR MONITORING OF FRP-STRENGTHENED BEAMS

Enrique Sevillano[*], Ricardo Perera[*], Ángel Arteaga[†], Ana De Diego[†]

*Technical University of Madrid
Department of Structural Mechanics
José Gutiérrez Abascal 2
28006 Madrid, Spain
e-mail: perera@etsii.upm.es

† Eduardo Torroja Institute for Construction Science (CSIC)
Department of Construction
Serrano Galvache, 4
28033 Madrid, Spain

Key words: FRP, Debonding identification, Simplified model, Fibre optic sensors.

Summary. *Advanced composite materials are increasingly used in the strengthening of reinforced concrete (RC) structures. The use of externally bonded strips made of fibre-reinforced plastics (FRP) as strengthening method has gained widespread acceptance in recent years since it has many advantages over the traditional techniques. However, unfortunately, this strengthening method is often associated with a brittle and sudden failure caused by some form of FRP bond failure, originated at the termination of the FRP material or at intermediate areas in the vicinity of flexural cracks in the RC beam. Up to date, little effort in the early prediction of the debonding in its initial instants even though this effect is not noticeable by simple visual observation. An early detection of this phenomenon might help in taking actions to prevent future catastrophes.*

Fibre-optic Bragg grating (FBG) sensors are able to measure strains locally with high resolution and accuracy. Furthermore, as their physical size is extremely small compared with other strain measuring components, it enables to be embedded at the concrete-FRP interface for determining the strain distribution without influencing the mechanical properties of the host materials.

This paper shows the development of a debonding identification methodology based on strains experimentally measured. For, it a simplified model is implemented to simulate the behaviour of FRP-strengthened reinforced concrete beams. This model is taken as a basis to. develop an model updating procedure able to detect minor debonding at the concrete-FRP interface from experimental strains obtained by using FBG sensors embedded at the interface.

1 INTRODUCTION

Advanced composite materials are increasingly used in the strengthening of reinforced concrete (RC) structures (Bank [1]). The use of externally bonded strips made of fibre-reinforced plastics (FRP) as strengthening method has gained widespread acceptance in recent years since it has many advantages over the traditional techniques, especially because of the high strength and modulus of elasticity, improved durability, and low weight of the composite material. Failure of FRP-strengthened RC beams may take a variety of forms including all those associated with conventional concrete beams. However, unfortunately, this strengthening method is often associated with a brittle and sudden failure caused by some form of FRP bond failure. This kind of failure is produced in the form of cover delamination, i.e., along the plane of the steel reinforcement, or FRP delamination, i.e., in the plane along the FRP-concrete interface. Furthermore, failure may be originated at the termination of the FRP material and propagate towards the midspan (Yang et al. [2], Pesic et al. [3]) or in the vicinity of flexural cracks in the RC beam and propagate towards the FRP termination (Sebastian [4], Yao et al. [5]). Hence, flexural cracking of the RC beam has a major influence on the overall response of the strengthened member, and it affects the distribution of the stresses in the various constituents of the strengthened member.

The topic of structural health monitoring has been scarcely developed in FRP strengthened RC beams in spite of its importance to prevent brittle failure modes. This work proposes a first approach to develop this topic which should be extended increasingly in the future. For it, a spectral finite element (SFE) model (Doyle [6]) is implemented in the framework of FRP-strengthened RC beams.

2 DIFFERENTIAL EQUATIONS

Considering first-order shear deformation theory, the axial and transverse displacement field can be expressed as:

$$u_C(x,z,t) = u_0(x,t) - z\phi(x,t) \tag{1}$$

$$u_{FRP}(x,z,t) = u_0(x,t) - z\phi(x,t) + s(x,t) \tag{2}$$

$$w(x,z,t) = w(x,t) \tag{3}$$

where u_C, u_{FRP} and w are respectively the axial displacements in RC beam and FRP plate and the transverse displacement at a material point, ϕ is the curvature-independent rotation of the beam cross-section about the Y-axis and s is the interface slip.

The linear constitutive model for the concrete beam and the FRP plate can be expressed as

$$\sigma_{xC} = E_C \varepsilon_{xC} \qquad \tau_{xzC} = G_C \gamma_{xzC} \tag{4}$$

$$\tau_{xzFRP} = G_{FRP} \gamma_{xzFRP} \tag{5}$$

where the material constants, E and G, are referred to the concrete beam (C) or the external plate (FRP) depending on the material considered.

Applying Hamilton's principle, the governing equations of the FRP flexural strengthened RC beam are obtained and can be written as

$$\delta u_0 : I_0\ddot{u}_0 - I_1\ddot{\phi} + I_{0FRP}\ddot{s} - A_{11}u_{0,xx} + B_{11}\phi_{,xx} - A_{FRP}s_{,xx} = 0 \tag{6}$$

$$\delta w : I_0\ddot{w} - A_{22}w_{,xx} + A_{22}\phi_{,x} = 0 \tag{7}$$

$$\delta\phi : I_2\ddot{\phi} - I_1\ddot{u}_0 - I_{1FRP}\ddot{s} + B_{11}u_{0,xx} - D_{11}\phi_{,xx} - A_{22}w_{,x} + A_{22}\phi + B_{FRP}s_{,xx} = 0 \tag{8}$$

$$\delta s : I_{0FRP}\ddot{s} + I_{0FRP}\ddot{u}_0 - I_{1FRP}\ddot{\phi} - A_{FRP}s_{,xx} - A_{FRP}u_{0,xx} + B_{FRP}\phi_{,xx} + \frac{G_{AD}sb_{AD}}{e_{AD}} = 0 \tag{9}$$

and associated force boundary equations can be expressed as

$$N = A_{11}u_{0,x} - B_{11}\phi_{,x} + A_{FRP}s_{,x} \tag{10}$$

$$V = A_{22}w_{,x} - A_{22}\phi \tag{11}$$

$$M = -B_{11}u_{0,x} + D_{11}\phi_{,x} - B_{FRP}s_{,x} \tag{12}$$

$$N^* = A_{FRP}s_{,x} + A_{FRP}u_{0,x} - B_{FRP}\phi_{,x} \tag{13}$$

where $(\cdot)$ denotes temporal derivative. N, V, M and N^* are the stress resultants associated with the variables u_0, w, ϕ and s, respectively.
A_{11}, B_{11}, D_{11}, A_{22}, A_{FRP} and B_{FRP} are the stiffness coefficients obtained from the material properties:

$$\left[A_{11}\ B_{11}\ D_{11}\right] = \int_{z_{C1}}^{z_{C2}} E_C\left[1\ \ z\ \ z^2\right]b_C\,dz + \int_{z_{FRP1}}^{z_{FRP2}} E_{FRP}\left[1\ \ z\ \ z^2\right]b_{FRP}\,dz + \sum_{j=1}^{NSS} E_{sj}A_{sj}\left[1\ \ z_j\ \ z_j^2\right] \tag{14}$$

$$\left[A_{22}\right] = \int_{z_{C1}}^{z_{C2}} G_C b_C\,dz + \int_{z_{FRP1}}^{z_{FRP2}} G_{FRP}b_{FRP}\,dz \tag{15}$$

$$\left[A_{FRP}\ B_{FRP}\right] = \int_{z_{FRP1}}^{z_{FRP2}} E_{FRP}\left[1\ \ z\right]b_{FRP}\,dz \tag{16}$$

3 FORMULATION OF THE SPECTRAL ELEMENT

A spectral Timoshenko beam finite element for the problem under consideration has been used. Using discrete Fourier transformation (DFT) for the temporal field, the spectral solution for the displacement field, $\{u\} = \left(u_0(x,t), w(x,t), \phi(x,t), s(x,t)\right)$, can be expressed as

$$\{u\} = \sum_{n=1}^{N}\left(\hat{u}_0(x,\omega_n), \hat{w}(x,\omega_n), \hat{\phi}(x,\omega_n), \hat{s}(x,\omega_n)\right)e^{-j\omega_n t} = \sum_{n=1}^{N}\left\{\hat{u}(x,\omega_n)\right\}e^{-j\omega_n t} \tag{17}$$

where $j = \sqrt{-1}$, ω_n is the circular frequency at the nth sampling point and N is the frequency index corresponding to the Nyquist frequency in FFT. The vector $\left\{\hat{u}(x,\omega_n)\right\}$ represents the spectral amplitude vector corresponding to the generic displacement vector as a function of x and ω_n.

By substituting the assumed solution of the displacement field in the governing equations, a set of ordinary differential equations is obtained for $\{\hat{u}(x,\omega_n)\}$, whose solution is of the form $\{\hat{u}^*\}e^{-jkx}$ where k is the wavenumber and $\{\hat{u}^*\}$ is a vector of unknown constants, i.e., $\{\hat{u}^*\}=(u_0^*,w^*,\phi^*,s^*)$.

3.1 Shape functions

After computing the wavenumbers at a particular frequency ω_n the generic displacement vector has the following form

$$\{\hat{u}(x,\omega_n)\}=\begin{pmatrix}\hat{u}_0(x,\omega_n)\\ \hat{w}(x,\omega_n)\\ \hat{\phi}(x,\omega_n)\\ \hat{s}(x,\omega_n)\end{pmatrix}=\begin{bmatrix}R_{11} & \dots & R_{18}\\ R_{21} & \dots & R_{28}\\ R_{31} & \dots & R_{38}\\ R_{41} & \dots & R_{48}\end{bmatrix}\begin{bmatrix}e^{-jk_1x} & 0 & \dots & 0\\ 0 & e^{-jk_2x} & \dots & 0\\ \vdots & \ddots & \ddots & \vdots\\ 0 & \dots & \dots & e^{-jk_8x}\end{bmatrix}\{A(\omega_n)\} \quad (18)$$

where $k_{p+4}=-k_p$ (p=1,…,4) are the wavenumbers. The above equation can be written in a compact way as

$$\{\hat{u}(x)\}_n=[R]_n[D(x)]_n\{A\}_n \quad (19)$$

where $[R]_n$ is the amplitude ratio matrix of size 4x8, $[D(x)]_n$ is a diagonal matrix whose ith element is e^{-jk_ix} and $\{A\}_n$ is a vector of eight unknown constants to be determined.

The eight unknown coefficients A_i can be calculated as a function of the nodal spectral displacements, by evaluating equation (18) at the two nodes of the element, i.e., at x=0 and x=L giving

$$\begin{pmatrix}\{\hat{u}_1\}_n\\ \{\hat{u}_2\}_n\end{pmatrix}=\begin{bmatrix}R\\ R\end{bmatrix}_n\begin{bmatrix}D(0)\\ D(L)\end{bmatrix}_n\{A\}_n=[T_1]_n\{A\}_n \quad (20)$$

where $\{\hat{u}_1\}_n$ and $\{\hat{u}_2\}_n$ are the nodal displacements of node 1 and node 2, respectively.

Solving (20) gives

$$\{A\}_n=[T_1]_n^{-1}\begin{pmatrix}\{\hat{u}_1\}_n\\ \{\hat{u}_2\}_n\end{pmatrix} \quad (21)$$

3.2 Dynamic stiffness

The dynamic stiffness matrix is formulated by using the force boundary conditions at the nodes of the element.

Con formato: Espacio Antes: 6 pto, Después: 6 pto, Punto de tabulación: 8 cm, Centrado + 16 cm, Derecha + No en 7,5 cm + 15 cm

Con formato: Fuente: Cursiva

Con formato: Fuente: Cursiva

Con formato: Fuente: Cursiva

Con formato: Fuente: Cursiva

Con formato: Fuente: Cursiva

Con formato: Izquierda, Espacio Antes: 6 pto, Después: 6 pto, Punto de tabulación: 8 cm, Centrado + 16 cm, Derecha + No en 7,5 cm + 15 cm

Con formato: Punto de tabulación: 16 cm, Derecha + No en 15 cm

The nodal spectral forces $\left\{\hat{f}\right\}_n = \left(\hat{N} \quad \hat{V} \quad \hat{M} \quad \hat{N}^*\right)_n^T$ can be expressed in terms of the unknown constants $\{A\}_n$ by differentiating the spectral displacements with respect to x in equation (18) and using the force boundary equations (10)-(13). Then, by evaluating the force vector at both nodes of the element the following expression is obtained

$$\begin{pmatrix} \left\{\hat{f}_1\right\}_n \\ \left\{\hat{f}_2\right\}_n \end{pmatrix} = \left[T_2\right]_n \{A\}_n \tag{22}$$

where $\left[T_2\right]_n$ is a matrix dependent on the stiffness coefficients and the wavenumbers and whose expression is

$$\begin{aligned} T_2(1,i) &= jk_j(A_{11}R(1,i) - B_{11}R(3,i) + A_{FRP}R(4,i)) \\ T_2(2,i) &= jk_j A_{22}R(2,i) - A_{22}R(3,i) \\ T_2(3,i) &= jk_j\left(-B_{11}R(1,i)\right) + D_{11}R(3,i) - B_{FRP}R(4,i)) \\ T_2(4,i) &= jk_j\left(A_{FRP}R(1,i) + A_{FRP}R(4,i) - B_{FRP}R(3,i)\right) \\ T_2(5:8,i) &= -T_2(1:4,i)e^{-jk_jL} \qquad i = 1,\ldots,8 \end{aligned} \tag{23}$$

Combining relations (21) and (22), the frequency dependent dynamic stiffness matrix $\left[K\right]_n$ at frequency ω_n for the proposed beam spectral finite element can be calculated as

$$\left[K\right]_n = \left[T_2\right]_n \left[T_1\right]_n^{-1} \tag{24}$$

and equation (22) becomes

$$\begin{pmatrix} \left\{\hat{f}_1\right\}_n \\ \left\{\hat{f}_2\right\}_n \end{pmatrix} = \left[T_2\right]_n \left[T_1\right]_n^{-1} \begin{pmatrix} \left\{\hat{u}_1\right\}_n \\ \left\{\hat{u}_2\right\}_n \end{pmatrix} = \left[K\right]_n \begin{pmatrix} \left\{\hat{u}_1\right\}_n \\ \left\{\hat{u}_2\right\}_n \end{pmatrix} \tag{25}$$

But the fundamental difference from the conventional FE method is that all the spectral amplitudes that correspond to element nodal variables are evaluated at each frequency step (FFT sampling points) instead of pseudo-static variables evaluated at each time step or at each eigenfrequency.

4 DAMAGE IDENTIFICATION

The model derived previously can be used to develop numerical algorithms for damage detection studies. Damage identification is essentially an inverse problem which requires the application of model updating techniques and the formulation of suitable objective functions. Performance of the procedure largely depends upon the objective function.

By means of a strain sensory system installed in the structure, a permanent control might be carried out. Furthermore, technologies such as Bragg grating-based fibre optic sensors make easier this process. This kind of sensors can provide a high sensitivity to debonding damage since can be easily embedded at the FRP-concrete interface with a minimum of perturbation to the surrounding material.

With this purpose, the sum of squared relative differences of static deformations at different locations of the structure might be employed to define the objective function:

$$F = \sum_{j=1}^{m} \left(\frac{\varepsilon_{\text{num}\,j}(d_e) - \varepsilon_{\text{exp}\,j}}{\varepsilon_{\text{exp}\,j}} \right)^2 \qquad e = 1, \ldots, NE \tag{26}$$

in which the subscript j represents the jth measurement within the set of measurements carried out under a load case and $\varepsilon_{\text{num}\,j}$ and $\varepsilon_{\text{exp}\,j}$ are the computed and measured responses, respectively.

The updating parameters, d_e, defined for each element, e, are the uncertain physical properties of the NE elements of the numerical model, in our case, the reduction factors or damage indices affecting to the RC-FRP interface stiffness.

To ensure the effectiveness of the procedure, strain profiles obtained for different loading cases might be considered which involves that different objective functions should be defined in the updating procedure, one for each loading.

5 PARTICLE SWARM OPTIMIZATION

The presence of multiple objectives requires finding the values of the damage parameter set $\{d\}$ that simultaneously minimize the objectives. A multi-objective problem, in principle, produces a set of optimal solutions known as Pareto-optimal solutions instead of a single optimal solution. Each point in the Pareto optimal solution set is optimal in the sense that improvement in one objective function leads to degradation in at least one of the remaining objective functions.

Evolutionary algorithms, such as genetic algorithms, are especially effective to solve multi-objective optimization problems. A multi-objective GA simultaneously minimizes multiple objective functions, rather than using arbitrary weighting factors to combine them to a single-objective function. As they search for a set of solutions in parallel, unlike conventional optimization techniques, they are particularly appropriate for solving multi-objective problems since the search process can be driven towards a family of solutions representing the set of Pareto optimal solutions.

Particle swarm optimization (PSO) [7] is one of the newest techniques within the family of optimization algorithms and is based on an analogy with the choreography of flight of a flock of birds. The PSO algorithm relies only on two simple PSO self-updating equations whose purpose is to try to emulate the best global individual found, as well as the best solutions found by each individual particle. Since an individual obtains useful information only from the local and global optimal individuals, it quickly converges to the best solution. PSO has become very popular because of its simplicity and convergence speed. Apparently, PSO has the same effectiveness as the GA but with better computational efficiency. Because of it, a multi-objective version of this algorithm has been used in this work.

6 NUMERICAL STUDY

To evaluate the methodology presented, a numerical study has been carried out in which a simulated damage scenario has been assumed and the 1D spectral element model presented in Section 2 has been used as numerical model in the proposal.

A very refined 2D finite element (FE) model has been used to generate the pseudo-experimental strains. This model would not be suitable for the damage detection algorithm due to its high computational cost. In the FE model, plane stress elements were used for the concrete, adhesive and FRP, while the internal steel reinforcement was modeled using truss elements. Loss of shear transfer in the debonded zones was simulated by reducing the mechanical properties of the adhesive. The geometric dimensions and the reinforcement layout in the sections are illustrated in Fig. 1 and the material properties used in the model were assigned as follows: a) for concrete and steel reinforcement, the elastic moduli were taken to be 25000 MPa and 210000 MPa, respectively, and their Poisson coefficients are 0.2 and 0.3; b) for FRP external reinforcement, the elastic modulus and Poisson coefficient were taken to be E=165000 MPa and υ=0.35, respectively; c) for adhesive, the shear modulus was assumed to be G=4300 MPa. Since only strains under service loads were used in the damage identification procedure, a linear elastic analysis was performed.

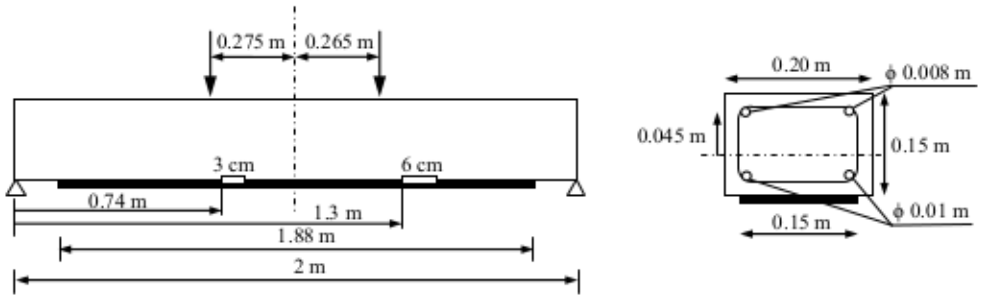

Figure 1: Geometrical properties of the FRP-strengthened beam

Initially, two sets of pseudo-experimental strains at the FRP strip of the undamaged structure were generated with the FE model by applying separately a concentrated load at two different locations, to a distance of 0.275 m and 0.265 m, respectively, from the middle section (Fig.1). The strains were measured at 17 points along the FRP strip and were used to update the proposed baseline 1D spectral model by using a two-objective problem with the objective functions defined according to Eq.(26). Once a baseline spectral model has been set, two new sets of pseudo-experimental strains at the FRP strip were generated with the FE model as previously but introducing simultaneously two artificial damages of length equal to 3 cm and 6 cm, respectively, at the FRP-concrete interface. The location of these two damage areas is shown in Fig.1. A two-objective optimization problem has been carried out again to identify

the debonded areas. Selected parameters for the application of the PSO algorithm are the following: Cognitive parameter $c_1 = 2$, social parameter $c_2 = 2$, initial inertia weight $w_{max} = 0.95$, final inertia weight $w_{end} = 0.4$, maximum velocity $v_{max} = 10$ 0. Twenty simulation runs were performed for each algorithm in order to study the statistical performance and a random initial population of 50 individuals was created for each of the 20 runs.
Fig.2 shows the damage distribution for the interfacial elements. This figure illustrates that the debonded zones (Elements 4 and 12) are easily identified. Furthermore, the detected severity is higher in the wider damaged area. With only a limited number of available strain readings the damage detection was performed in a simple and fast way compared to the large number of elements involved in a finite element analysis. Of course, the reliability of the method would improve in field monitoring by using more measurement points.

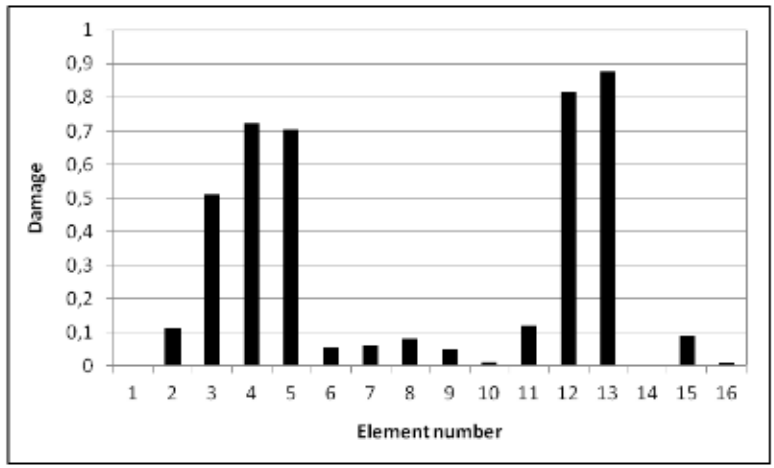

Figure 2: Damage estimation for the FRP-strengthened beam

7 CONCLUSIONS

A multi-objective model updating procedure using spectral elements has been implemented to monitor the integrity of the adhesive bond between the laminate and concrete of FRP-strengthened beams. Static strains measured by employing Bragg type fibre optic sensors can be used to develop the procedure allowing a high number of readings with only a single cable embedded within the concrete-FRP interface.

ACKNOWLEDGEMENTS

The writers acknowledge the support for the work reported in this paper from Spanish Ministry of Economy and Competitivity (project BIA2010-20234-C03-01). Financial support for the FPI research fellowship given to Enrique Sevillano is also acknowledged.

REFERENCES

[1] Bank, LC. *Composites for construction: Structural design with FRP materials*, first ed. John Wiley and Sons, 2006.

[2] Yang, ZJ, Chen, JF, Proverbs, D. Finite element modelling of concrete cover separation failure in FRP plated RC beams, *Construction and Building Materials* 17 (1), 3-13, 2003.

[3] Pesic, N, Pilakoutas, K. Concrete beams with externally bonded flexural FRP-reinforcement: analytical investigation of debonding failure, *Composites Part B-: Engineering* 34(4), 327-338, 2003.

[4] Sebastian, WM. Significance of midspan debonding failure in FRP-plated concrete beams, *Journal of Structural Engineering ASCE* 127(7), 792-798, 2001.

[5] Yao, J, Teng, JG, Lam, L. Experimental study on intermediate crack debonding in FRP-strengthened RC flexural members, *Advances in Structural Engineering* 8 (4), 365-396, 2005.

[6] Doyle, JF, *Wave Propagation in Structures*, first ed. Springer, New York, 1997.

[7] Kennedy, J, Eberhart RC. Particle swarm optimization. Proceedings of IEEE International Conference on Neural Networks, Piscataway, New Jersey, 1942-1948, 1995.